Au$_{67}$(SR)$_{35}$ Nanomolecules: Characteristic Size-Specific Optical, Electrochemical, Structural Properties and First-Principles Theoretical Analysis

Praneeth Reddy Nimmala,[†] Bokwon Yoon,[‡] Robert L. Whetten,[§] Uzi Landman,[‡] and Amala Dass[†,*]

[†]Department of Chemistry and Biochemistry, University of Mississippi, University, Mississippi 38677, United States
[‡]School of Physics, Georgia Institute of Technology, Atlanta, Georgia 30332-0430, United States
[§]School of Chemistry and Biochemistry, Georgia Institute of Technology, Atlanta, Georgia 30332, United States

S *Supporting Information*
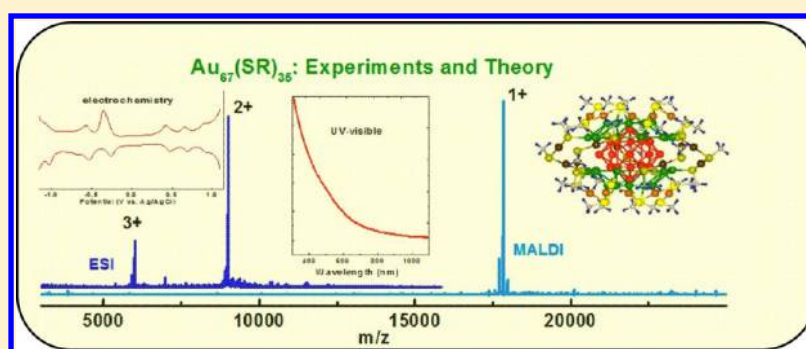
ABSTRACT: The preparation of gold nanomolecules with sizes other than Au$_{25}$(SR)$_{18}$, Au$_{38}$(SR)$_{24}$, Au$_{102}$(SR)$_{44}$, and Au$_{144}$(SR)$_{60}$ has been hampered by stability issues and low yields. Here we report a procedure to prepare Au$_{67}$(SR)$_{35}$, for either R = −SCH$_2$CH$_2$Ph or -SC$_6$H$_{13}$, allowing high-yield isolation (34%, ∼10-mg quantities) of the title compound. Product high purity is assessed at each synthesis stage by rapid MALDI−TOF mass-spectrometry (MS), and high-resolution electrospray-ionization MS confirms the Au$_{67}$(SR)$_{35}$ composition. Electronic properties were explored using optical absorption spectroscopy (UV−visible−NIR regions) and electrochemistry (0.74 V spacing in differential-pulsed-voltammetry), modes of ligand binding were studied by NMR spectroscopy (^{13}C and ^{1}H), and structural characteristics of the metal atom core were determined by powder X-ray measurements. Models featuring a Au$_{17}$ truncated-decahedral inner core encapsulated by the 30 anchoring atoms of 15 staple-motif units have been investigated with first-principles electronic structure calculations. This resulted in identification of a structure consistent with the experiments, particularly, the opening of a large gap (∼0.75 eV) in the (2−) charge-state of the nanomolecule. The electronic structure is analyzed within the framework of a superatom shell model. Structurally, the Au$_{67}$(SR)$_{35}$ nanomolecule is the smallest to adopt the complete truncated-decahedral motif for its core with a surface structure bearing greater similarity to the larger nanoparticles. Its electronic HOMO−LUMO gap (∼0.75 eV) is nearly double that of the larger Au$_{102}$ compound and it is much smaller than that of the Au$_{38}$ one. The intermediary status of the Au$_{67}$(SR)$_{35}$ nanomolecule is also reflected in both its optical and electrochemical characteristics.

INTRODUCTION

Gold nanomolecules are ultrasmall (<2-nm) gold nanoparticles of molecular definition and atomic monodispersity,[1−9] with molecular formulas such as Au$_{25}$(SR)$_{18}$, Au$_{38}$(SR)$_{24}$, and Au$_{144}$(SR)$_{60}$. Each contains a distinct number of gold atoms protected by a specific number of thiolate ligands. They differ in certain respects from their larger metallic, or plasmonic, counterparts which commonly are taken to have core diameters larger than 2 nm (∼200 atoms). For example, while for gold particles with sizes of ∼2 nm[8,9] a strong, broad, peak centered near 500 nm called the surface plasmon resonance (SPR) band emerges (resulting from collective response of the conduction electrons to the excitation), gold nanomolecules of smaller size show discrete, molecule-like electronic properties with an

enhanced electrochemical and optical HOMO−LUMO gap.[1−3] The 76.3 kDa atomically monodisperse, giant gold nanomolecule, named Faradaurates,[8] in honor of Michael Faraday's seminal 1857 work,[10] is the smallest size that supports the SPR peak. Smaller compounds (<2-nm) show size-specific features in the absorption spectrum with a common inflection at 1.7 eV for most of them. These unique features are attributed to single electron excitations rather than collective response. Similarly, the electrochemical behavior changes with size from the "Coulomb-staircase" quantized charging of a small capacitive

sphere to an irregular pattern with a HOMO−LUMO gap. The interesting size dependent optical and electronic properties of these nanomolecules can be attributed to quantum confinement effects and to the atomic packing.[4,5] Their stability can be explained by electronic[6] and geometric[1,7] effects.

Research in this field has crossed the milestone of determining the atomic structure by single crystal X-ray diffraction methods, first in the case of $Au_{102}(p\text{-MBA})_{44}$ (p-MBA refers to $para$-mercapto benzoic acid) followed closely by $Au_{25}(SCH_2CH_2Ph)_{18}$.[11−14] Certain conclusions about the structure−property relations in these compounds have been drawn from their atomic packing in the cluster core (or kernel) and also the Au−S bonding at the surface. This has indeed accelerated research in this field considerably, but the high yield synthesis of monodisperse gold thiolate nanomolecules remains as a major challenge hindering the use of these nanomolecules in practical applications.

So far, only a few such gold nanomolecules with core masses of 5, 8, 14, 22, 29, and 76 kDa have been synthesized and identified.[4] These represent mass of the inorganic core atoms (Au and S) only, identified by earlier laser desorption ionization (LDI) studies, and correspond to 25, 38, 67, 102, 144 and ∼330 atoms, respectively. For example, the 5 kDa referred to $Au_{25}(SR)_{18}$ with a parent ion mass of 7.394 kDa for phenylethanethiolate.[15] It is essential that one classifies these nanomolecules on the basis of both mass and composition, as these relate to the varying ratio of gold to thiolate groups on which many properties depend. Of these compounds, the 5, 8, and 29 kDa nanomolecules ($Au_{25}(SR)_{18}$, $Au_{38}(SR)_{24}$, and $Au_{144}(SR)_{60}$ respectively; hereafter referred to as Au_{25}, Au_{38}, and Au_{144}) are stable under harsh thermochemical treatment,[16] facilitating straightforward synthesis-isolation procedures. Consequently, a number of (reproducible) experimental and theoretical reports[6,17−21] on the selected 25-, 38- and 144-atom compounds have appeared.[22] Organic soluble versions of other core sizes, such as ∼Au_{68} (14 kDa) and Au_{102} (22 kDa), however, are not so well studied. The latter has been studied more from the crystal structure of its water-soluble analogue.[23]

Nanomolecules related to the title compound were first studied as enriched 14 kDa fractions, and were suggested to contain ∼75 Au atoms based on LDI mass spectra.[4,24] Analysis of X-ray scattering measurements indicated a core structure modified from the bulk fcc lattice by 5-fold twinning, consistent with a truncated-decahedral (m-Dh) morphology.[25] Among other properties initially explored were its electrical (voltammetric) and optical responses,[2] which were interpreted as consistent with an optical absorption onset near ∼0.6 eV.[5] Recently some of us reported the preparation of samples enriched in 14 kDa species (containing minor amounts of 25- and 102-atom compounds), and assigned its composition as $Au_{68}(SR)_{34}$ on the basis of the detection of the parent molecular ion by a much gentler method, matrix-assisted laser desorption ionization (MALDI) mass spectra.[26] In recent reports, it has usually been regarded merely as an intermediate product,[27] and its characterization has remained incomplete due to lack of methods to isolate this nanomolecule in pure form in sufficient quantities.

Here, we report for the first time not only the high-yield synthesis and isolation of the pure title compound but also the determination of its composition as $Au_{67}(SR)_{35}$ on the basis of high resolution electrospray (ESI) mass spectrometry on two different thiolate groups, namely, 2-phenylethanethiol and n-hexanethiol. New voltammetric experiments on the purified

compound reveal a large central electrochemical gap of 0.74 V that is unique to the 67-atom core, yet falls neatly within the size-dependent behavior of earlier results on much studied Au_{25}, Au_{38}, and Au_{144} nanomolecules. Further characterization was performed using optical absorption (UV−visible−NIR) spectroscopy, NMR spectroscopy, powder XRD diffraction measurements, which permit a deduction of its structural characteristics. High level electronic structure theory, applied to candidate structural-models that are consistent with the evidence as well as chemical-bonding precedents, has identified a remarkable structure that can account for the high stability and offers deep insight into the characteristic structure, bonding and electronic structure underlying the singular electrochemical and optical properties.

Analysis of the joint experimental and theoretical investigations described in this paper, resulted in identification of a structure consistent with experiments, particularly the opening of a large gap (∼0.75 eV) in the (2−) charge-state of the nanomolecule, similar to the anionic state of the smaller $[Au_{25}(SR)_{18}]^{1-}$ gold nanomolecule.[15] Structurally, the $Au_{67}(SR)_{35}$ nanomolecule is the smallest to adopt the complete truncated-decahedral motif for its core with a surface structure bearing greater similarity to the larger nanoparticles. Its electronic HOMO−LUMO gap (∼0.75 eV) is nearly double that of the larger Au_{102} compound, and it is much smaller than that of the Au_{38} one. The intermediary status of the $Au_{67}(SR)_{35}$ nanomolecule is also reflected in both its optical and electrochemical characteristics.

EXPERIMENTAL METHODS

Chemicals. Phenylethyl mercaptan (SAFC, ≥ 99%), sodium borohydride (Acros, 99%), $trans$-2-[3-(4-$tert$-butylphenyl)-2-methyl-2-propenylidene]malononitrile (DCTB matrix) (Fluka, ≥ 99%) were purchased from Aldrich. Tetrahydrofuran (Acros anhydrous, stabilized 99.9%) and other solvents like toluene, methanol, acetonitrile and acetone were used from Fisher as received.

Equipment. UV−visible absorption spectra were recorded in toluene on a Shimadzu UV-1601 instrument. Matrix-assisted laser desorption time-of-flight (MALDI−TOF) mass spectra were collected on a Bruker Autoflex I mass spectrometer in linear positive mode using a nitrogen laser (337 nm) using DCTB as a matrix.[15] ESI−MS spectra were acquired on Waters SYNAPT HDMS instrument either with or without cesium acetate as an electrolyte. NMR spectra were recorded on a Bruker AC-300 NMR spectrometer at ∼10 mg/mL concentration. Electrochemical measurements were performed on a CHI 620 instrument using 5 mg of title compound in 5 mL of THF solution with 0.5 M $TBAPF_6$ as supporting electrolyte under nitrogen atmosphere. Powder XRD measurements were performed on Bruker D8-Focus XRD instrument on a quartz substrate. 10 mg of sample was dissolved in minimal amount of toluene and deposited on the substrate and air-dried.

Synthesis and Isolation of $Au_{67}(SR)_{35}$ Nanomolecules. Briefly, the synthesis and isolation of $Au_{67}(SCH_2CH_2Ph)_{35}$ (hereafter as Au_{67}) proceeds via three stages. The $first$ stage is a single phase reaction using tetrahydrofuran (THF) as a solvent,[26−28] yielding a mixture rich in the 14 kDa and 22 kDa compounds. The $second$ stage involves mild thermochemical treatment of the polydisperse mixture obtained from the previous stage, in the presence of excess thiol,[24] to yield samples characterized by distinct peaks at 14 and 22 kDa with a good baseline separation (see Methods, below). The $third$ and
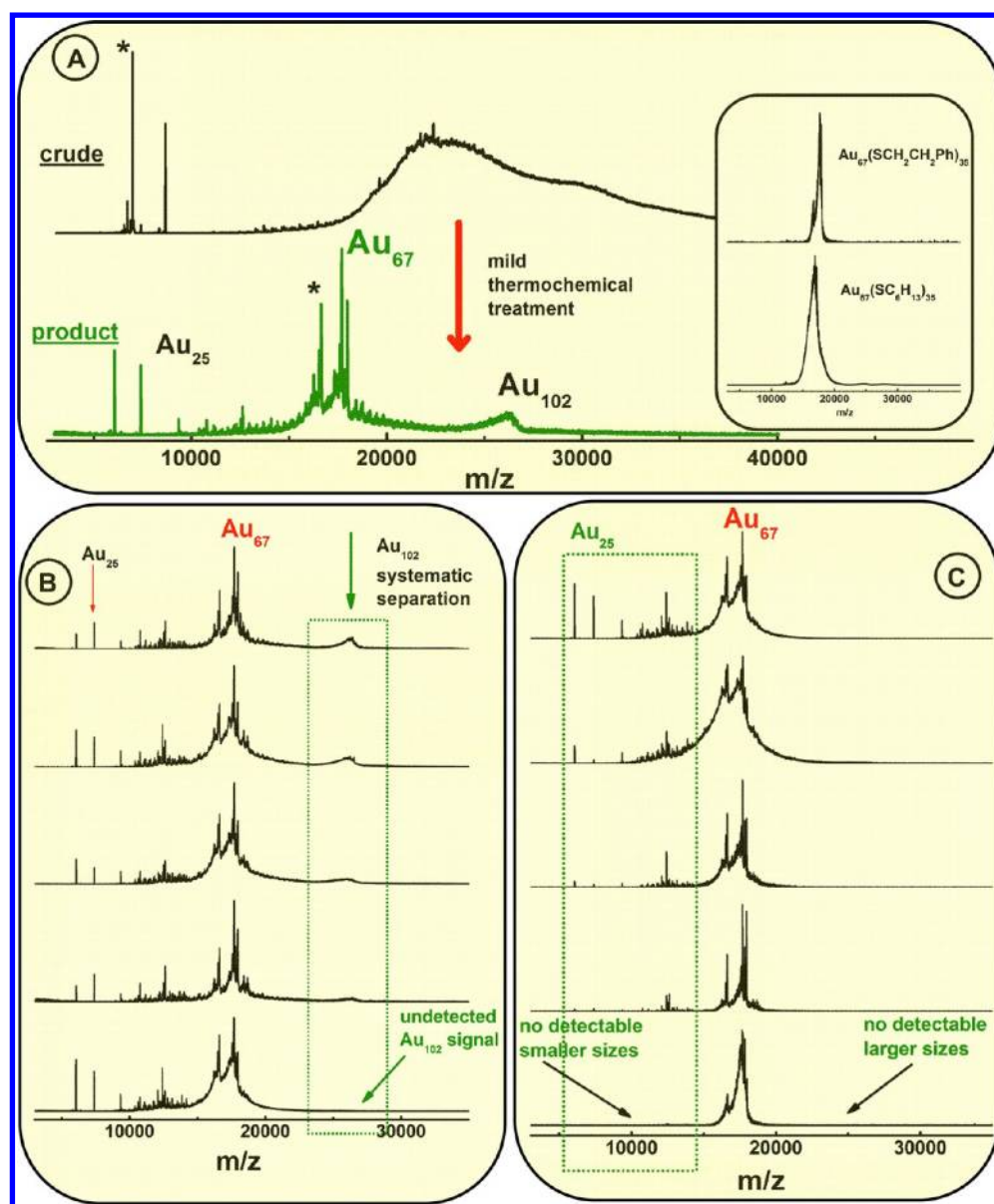
Figure 1. (a) Typical reaction where the initial crude product (control − top MALDI−MS spectrum) was subjected to mild thermo-chemical treatment to obtain a product (bottom MALDI−MS spectrum) where Au_{67} is a major products and other sizes are diminished in signal. Peaks with asterisk denotes fragments. (b) $Au_{67}(SR)_{35}$ purification separating larger clusters: MALDI spectra showing the systematic separation (top to bottom) of Au_{102} clusters from a mixture of Au_{25}, Au_{67}, and Au_{102}. The final product (bottom) is further used to separate the clusters lower in mass than $Au_{67}(SR)_{35}$. (c) $Au_{67}(SR)_{35}$ purification separating smaller clusters: Continuation of the separation process to remove sizes smaller than $Au_{67}(SR)_{35}$. Inset to part a: MALDI spectra of the pure $Au_{67}(SR)_{35}$ with two different ligands phenylethanethiol (top) and hexanethiol (bottom) taken at very high laser fluence. At high laser fluence, even minor amounts of impurities or other core size clusters will show higher signal intensity.

final stage involves multiple separation steps, described below, to remove the 22 kDa and any other species present in the product of second stage, to achieve the desired purity of Au_{67}.

We exploit the size-dependent solubility properties of gold nanoclusters through solvent fractionations[4] in order to isolate the 14 kDa compound. Control of the differential solubility allows for a neat separation of any single nanomolecule from a mixture of Au_{102}, Au_{67}, Au_{38}, and Au_{25}. We observed that toluene-acetone solvent mixtures, in certain proportions, precipitate Au_{102} leaving Au_{67} in the soluble part (for details see below). Similarly, the THF and methanol mixture in certain proportions precipitates Au_{67} and leaves smaller compounds like Au_{25} and Au_{38} in solution. In the isolation of Au_{67}, we observed that the THF−methanol solution (in different

proportions) was the most useful solvent mixture. The proportion of THF−methanol solution depends on the concentration of starting material mixture, drop, or addition rate of the nonsolvent methanol, stirring rate of the solution and polar/nonpolar differences in the nature of the protecting ligand used in synthesizing the nanomolecule. For example, we dissolved 100-mg of a crude mixture containing Au_{67} and Au_{102} in 1.0 mL of THF and added 0.8 mL of methanol at 1 drop/ minute to precipitate out the higher M.W. compound Au_{102}. Above all, like other separation methods,[29,30] this method does not yield pure product in a single fractionation and thus needs multiple fractionations to obtain the pure product. This initially laborious process, once implemented as a practical procedure, has become a fairly routine operation in our laboratory. In the

absence of a single-step synthesis of Au_{67}, this multistep solvent fractionation can yield highly pure $Au_{67}(SR)_{35}$ nanomolecules (~10-mg per batch quantities). As shown below, "purity" refers here to the absence of other size nanomolecules within the detection limit of MALDI−TOF and ESI-Q−TOF mass spectrometers.

Synthesis. *Step 1: Synthesis of Crude Product.* Typically, 0.5 mmol of $HAuCl_4\cdot3H_2O$ was dissolved in 20 mL of THF and stirred for about 10 min before adding 6 mmol of phenylethanethiol ($PhCH_2CH_2SH$). The reaction mixture starts to change its color from golden yellow to turbid in about 15 min when stirred at 500 rpm). Then, we add 5 mmol of $NaBH_4$ to the reaction mixture. The color of the reaction mixture turned black. The stirring was continued for another 5 min and then the solvent was removed from the reaction mixture by rotary evaporation as quickly as possible. Once the solvent is completely removed, the resulting product, which was adhering to the round-bottom flask, was washed with methanol two or three times to remove the excess thiol and other soluble reaction byproducts. At this stage, the MALDI mass spectrometric analysis of this crude product shows a broad peak ranging in mass (see Figure 1a, top spectrum).

Step 2: Mild Thermo-Chemical Treatment of Au_{67} and Au_{102} Mixture. The synthesis of crude products does not yield the final product, the MALDI−MS may show a broad peak ranging in m/z value of 15 kDa to 25 kDa. In fact, this broad peak is typical of many reactions involving synthesis of the crude mixtures in step 1. In such cases, it is difficult to proceed for solvent fractionations as the baseline between the two clusters Au_{67} (18 kDa) and Au_{102} (26 kDa) is not perfectly resolved; in other words, there may be other metastable clusters other than Au_{67} and Au_{102}. The peaks of interest, Au_{67}, can often be sharpened by a mild thermochemical treatment.[24] This is accomplished by heating the product of stage 1 (≈100 mg) in 0.5 mL of toluene and 0.2 mL of phenylethanethiol at 60 °C for 1 h. This treatment flattens the baseline (see Figure 1a, bottom) between the stable clusters (Au_{67} and Au_{102}) and makes it suitable for solvent fractionations (step 3). Harsh chemical conditions (higher temperature or longer reaction time) must be avoided for this step, as they may result in decomposition of the species of interest.

Isolation. *Step 3: Solvent Fractionations To Get Pure Au_{67}.* Figure 1b tracks the systematic isolation or removal of Au_{102} from a mixture resulting in step 2. Since Au_{102} (~26 kDa) is larger in size (and more nonpolar ligands around it) compared to Au_{67} (~18 kDa) and other lower clusters, it can be removed successfully in a few fractionations using tetrahydrofuran and methanol. A typical solvent fractionation procedure involves dissolving the initial nanocluster mixture in a round-bottom flask in a least possible amount (~0.5 mL for 50 mg) of a nonpolar solvent like toluene or THF followed by addition of a polar solvent like methanol dropwise (~1 drop/minute). The lesser the drop rate of the polar solvent, the better the separation. But the time for completion will be longer. So the parameters are adjusted as per the requirements of each fractionation. The mixture in the round-bottom flask needs to be stirred at a constant rate (typically 300 rpm) which is high enough to mix the solvents homogenously, and slow enough to allow for precipitation of higher clusters. As the polarity of the mixture increases, the higher clusters (containing more nonpolar ligands) start precipitating. In general, *slower separation over longer time* periods yield better separation and results. So in the mixture of Au_{102}, Au_{67}, and Au_{25}, the heaviest

cluster (Au_{102}) precipitates out first. When a considerable amount of precipitate is seen at the bottom of the round-bottom flask, we stopped the stirring, allowed it to settle for a few minutes and then separate the soluble part from the insoluble part using a glass pipet. We then quickly analyze both the soluble and insoluble portions by MALDI−MS. A controlled first solvent fractionation shown in the figure below would result in a soluble part with most of the Au_{67} retained in it, while the precipitate would contain a major amount of Au_{102} with a little Au_{67}. We repeated these fractionations until we reached a stage where the soluble part has no MALDI detectable Au_{102}. This final soluble part (the bottom most spectra in Figure 1b is then used to remove the lower clusters and finally get pure Au_{67}.

Separating Lower Clusters. In Figure 1c, we show the systematic removal of all the lower molecular weight compounds compared to Au_{67}. Here again, solubility differences was used as that of Au_{102} separation above, except that this time the heaviest molecule in the mixture is Au_{67}. We have used THF to wet and dissolve the starting mixture and then gradually add methanol to it so far that almost all of the mixture has precipitated. The soluble portion now looks reddish in color and is very dilute (reddish color indicates the presence of low mass species like Au_{25}). This soluble fraction is then removed from the round-bottom flask and the precipitate is now ready for a second fractionation. Considering the area under the curve for each cluster in the starting material, the total amount of lower clusters is very small compared to Au_{67}. This means that there is more margin for error in the separation of lower molecular weight compounds. The drop rate can be relatively faster (2−3 drops/minute). These separations can be fast and simple. These fractionations were repeated until no peaks were detected in MALDI for lower molecular weight species even at high laser fluence (Figure 1a, inset).

■ EXPERIMENTAL RESULTS

Selected molecular properties of the purified title compound are collected in Table 1. The broad *size-purity* of the final

Table 1. Properties of $Au_{67}(SR)_{35}$ Nanomolecules

molecular weight of $Au_{67}(SCH_2CH_2Ph)_{35}$	17,999.56 (calcd), 17,999 (expt)
molecular weight of $Au_{67}(SC_6H_{13})_{35}$	17,299.57 (calcd), 17,301 (expt)
color	brown
solubility	true solutions in toluene, CH_2Cl_2, THF
electrochemical gap	0.74 V
stability	stable in air, moisture; and heating up to 50 °C; unstable while heating in the presence of excess thiol

products is determined principally by *MALDI−TOF mass spectrometry*. Figures 2a and 2b shows the MALDI−TOF mass spectra of the purified title compound showing 1+ peaks for phenylethanethiolate (light blue curve) and *n*-hexanethiolate (light red curve) ligands. In contrast to our earlier work,[26] here the analysis of the purified sample shows negligible intensity corresponding to Au_{25} or Au_{102}, around 7.3 and 26 kDa mass regions, respectively. For an elaboration of these methods including the multistep mass spectrometry based purification process, see the preceding section: Methods.
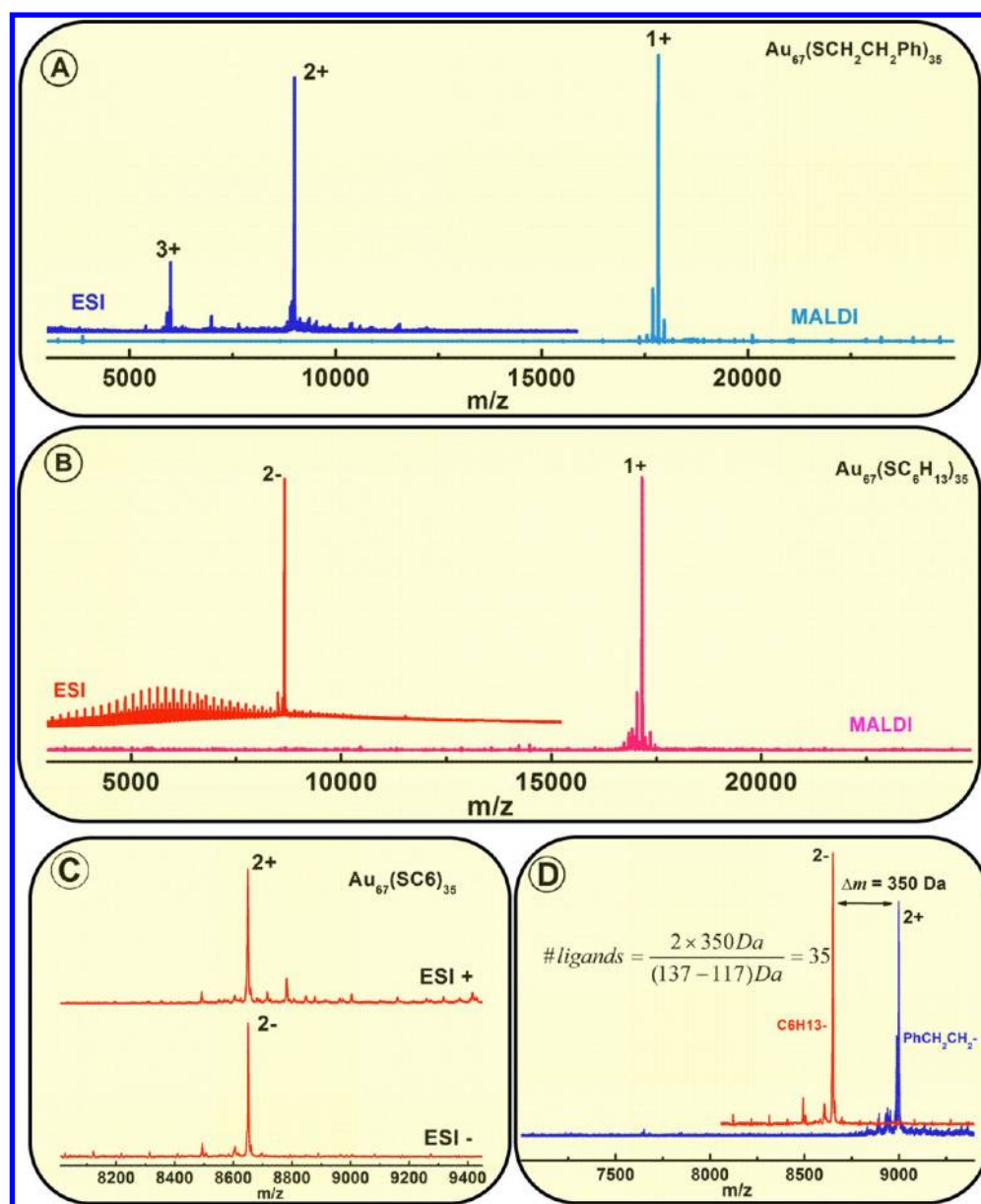
Figure 2. (A) Positive mode MALDI−TOF mass spectra(MS) (in light blue) and ESI−MS (dark blue) of $Au_{67}(SCH_2CH_2Ph)_{35}$ nanomolecules. (B) Positive mode MALDI−TOF−MS (in light red) and the negative mode ESI−MS of $Au_{67}(SC_6H_{13})_{35}$. (C) Positive mode (top) and negative mode (bottom) ESI mass spectra of $Au_{67}(SC_6H_{13})_{35}$. (D) ESI mass spectra of $Au_{67}(SR)_{35}$ nanomolecules protected by phenylethanethiolate (blue) and *n*-hexanethiolate (ligands) showing a mass difference of 350 Da used to calculate the number of ligands in the Au_{67} to be 35.

The *composition* of the nanomolecules is determined by *ESI−MS mass spectrometry* of the phenyl-ethane and hexanethiolate analogues. Figure 2a includes an ESI−MS spectrum (dark blue curve) of the title compound prepared using 2-phenyl-ethanethiol, which is dominated by peaks assigned to the multiply charged (2+ and 3+) parent ion. The multiply charged ions are lower in mass-to-charge ratio compared to singly charged species, and generally have better sensitivity, resolution and accuracy. The lower mass range and better resolution, due to multiply charged peaks, also offers a calibration check against previously known $Au_{25}(SR)_{18}$ and $Au_{144}(SR)_{60}$, which were employed here. The deconvolution of 3+ (5,999.5 Da/z) and 2+ (8,999.5 Da/z) peaks indicates that the singly charged parent ion mass, or molecular weight, is 17 999 Da. This may be compared with the value 17 999.5 Da, calculated from the molecular formula of the title compound using isotopic masses

and natural abundances. Note that this differs significantly from the earlier 18 059 Da value that was based solely on the MALDI−TOF−MS method and instrument.[26]

In order to conduct a critical test of the composition, we synthesized the title compound with a second thiolate ligand, *n*-hexanethiol, of different mass. Assuming this ligand also produces the nanomolecule with the same number of Au atoms and thiolate ligands, then the mass difference of the parent ions can be used to calculate the number of ligands.[31] An ESI mass spectrum of the *n*-hexanethiolate protected nano-molecule is shown in Figure 2b (red curve). It shows a 2− peak at 8650.5 Da/z. The deconvolution of this peak yields a 1− parent ion at 17 301 Da, in agreement with the calculated value (see Table 1).

We further observed that identical peaks were obtained for both positive and negative modes at 8650 Da/z, as shown in

Figure 2c. This is crucial because the ESI process often yields gas phase analyte ions with a counterion adduct. For example, $Au_{25}(SR)_{18}$ ions were observed with Cs, Rb, K, Na, and Li alkali-metal ion adducts[32] or tetraoctylammonium ion adducts,[33] in positive mode, while the negative mode exclusively yields the native $Au_{25}(SR)_{18}^-$ ion.[34] Similar results (not shown here) were also observed for the case of phenylethanethiolate protected nanomolecules.

Having established that the ESI mass spectra reflect parent molecular ions that are free of counterions, we used the 20-Da mass difference between 2-phenylethanethiolate (137 Da) and n-hexanethiolate (117 Da) protected nanomolecules to calculate the number of ligands. As detailed in Figure 2d, a mass difference, Δm of 350 Da/z for the $z = 2$ peaks would correspond precisely to 35 ligands.[35]

The unique composition (67,35) thus explains both the calibrated total masses observed and the difference (700 Da) arising from the two distinct thiolate ligands. One may henceforth regard this as a direct determination of the definite composition underpinning the 14-kDa class of cluster compound, much as the compositions (25,18) and (38,24) have defined the respective lower mass-ranges.

However, unlike the smaller nanomolecules, the new mass spectral results shown here do *not* indicate a definite charge state for the compound as produced in the solution-phase synthetic procedure. From the mass spectra shown in Figure 2, it is clear that charge states such as 2+, 3+, and 2− are observed for the $Au_{67}(SR)_{35}$ nanomolecules. [Other ESI−MS experiments with added cesium acetate electrolyte (not shown here) detect the compound in other charge states, including 1+ and the otherwise undetectable neutral, $z = 0$.] Therefore, we conclude that as the size of the nanoparticle gets larger, a number of different charge states can exist; these may be attributable to redox processes, as has been shown in detail for $Au_{25}(SR)_{18}$ (refs 32 and 33).

The *optical spectroscopic* characterization of the purified Au_{67} compounds has principally involved linear absorption spectroscopy of the dilute solutions in the UV−vis−NIR regions, covering the wavelengths ranging from 300 to 1100-nm, or 1.1−4.0 eV photon energy, with additional measurements to 1500 nm. In Figure 3, a typical UV−visible−NIR spectrum of Au_{67} is compared to that of a smaller Au_{38} and also a larger gold particle containing about 330 atoms. Under these conditions, the UV−visible spectrum of Au_{67} appears as a nearly monotonically rising curve, other than minor step-like features and a shoulder around 590 nm (2.1 eV). The expected onset of enhanced absorption is observed around 800 nm (~1.6 eV).[4,36] These features were also observed in Au_{67} protected by hexanethiol (see the Supporting Information). The spectrum is Figure 3 is in substantial agreement with that reported by Alvarez et al.[36] as analyzed further in Chen et al.[2] and Wyrwas et al.[5]

The *electrochemical characterization* of the purified Au_{67} compounds was performed by cyclic voltammetry (CV) and differential pulsed voltammetry (DPV). Figure 4a shows typical DPV results for $Au_{67}(SCH_2CH_2Ph)_{35}$ and the corresponding CVs are shown in Figure S1, Supporting Information. Six distinct features are noted, each corresponding to reversible single-electron redox waves; these are neatly spaced around a large central gap. Taking the charge-state in this region as a reference state, these transitions may be regarded as three oxidation peaks centered at {+0.48, +0.70 and +0.95 V} and three reduction peaks centered at {-0.26, −0.53, and −1.03 V}.
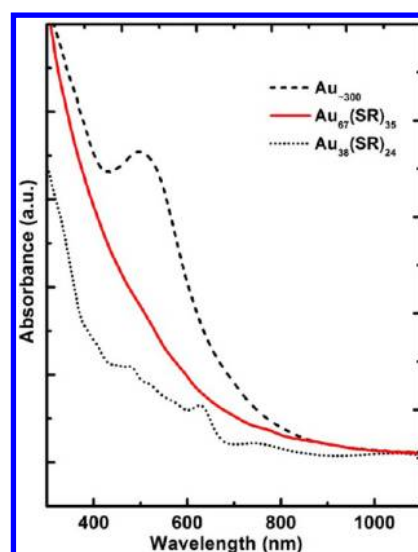

Figure 3. UV−visible optical spectrum of $Au_{67}(SR)_{35}$ nanomolecules (red) in toluene compared with a smaller cluster $Au_{38}(SR)_{24}$ (dotted) and a larger $Au_{\sim 300,}$ 76.3 kDa cluster (dashed).

The potential difference between the first oxidation and first reduction peaks, approximately 0.74-V, pertains to the central electrochemical gap. The potential difference between successive oxidation peaks and two reduction peaks (0.22 and 0.27 V respectively), provides an estimate of the "charging energy". Subtracting the electrochemical potential gap for charging energy, one obtains an estimate for the 'electronic gap' for this molecule-like compound to be ~0.5 eV. This analysis of the electronic and capacitive charging energies is (i) consistent with earlier results of Chen et al. obtained from samples where the 14 kDa species is not well isolated;[2] (ii) consistent with that deduced from optical analysis (see below); and (iii) less when compared to the energy gaps of its smaller counterparts Au_{25} and Au_{38}, but much larger than for Au_{144} (refs 37 and 38). The Au_{67} species thus fits the size dependent trend in the calculated HOMO−LUMO gaps as reported by Murray.[3] As the core size of the nanomolecule increases, the electrochemical gap disappears leading to (Coulomb staircase) quantized charging behavior.[37,39−43]

Evidence pertaining to the *ligand environments* of the pheynylethanethiolate groups of the highly purified $Au_{67}(SCH_2CH_2Ph)_{35}$ has been obtained by ^1H and ^{13}C *NMR spectroscopy* in dilute solutions. The ^1H NMR spectrum of the free $PhCH_2CH_2SH$ shows distinct peaks at 2.9 ppm due to methylene protons and near 7 ppm due to aromatic protons. Corresponding features are observed in the ^1H NMR of Au_{67}. This indicates that these thiolate ligands are bound to the gold core. The methylene proton peaks at around 3 ppm are broadened, which is expected for a larger compound. The broadening of the peaks increases with increasing proximity of the methylene proton to the sulfur headgroup bonded to the gold surface.[44] The ^{13}C NMR spectrum similarly strengthens the case for chemisorption of thiolate groups on the gold surface. Figure 5 shows the carbon peaks of the compound $Au_{67}(SCH_2CH_2Ph)_{35}$ in comparison with that of the reference $PhCH_2CH_2SH$. (The triplet at around 80 ppm is due to the solvent $CDCl_3$.) The peaks in the 130 ppm range are due to the aromatic carbons. The peaks between 20 and 40 are due to the methylene carbons. These methylene carbons are the ones which interact strongly with the gold surface and are therefore
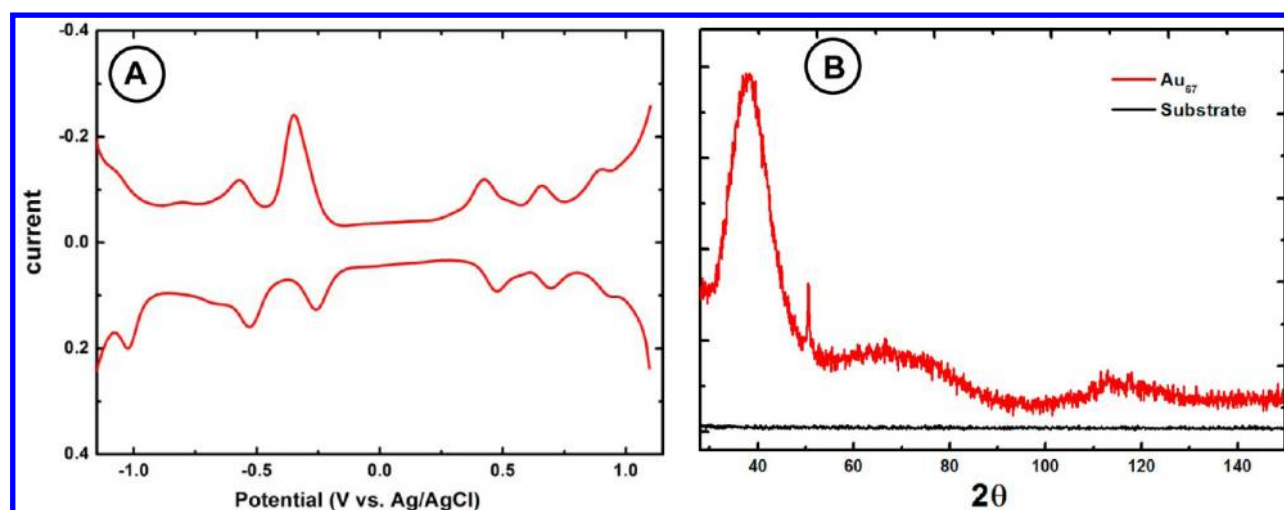
Figure 4. (a) Differential pulse voltammetry of $Au_{67}(SCH_2CH_2Ph)_{35}$ nanomolecules in THF solvent/0.5 M TBAPF$_6$ supporting electrolyte (see the Supporting Information for related cyclic voltammograms). (b) Powder X-ray diffraction pattern of $Au_{67}(SCH_2CH_2Ph)_{35}$ nanomolecules (red) in comparison with that of a blank quart substrate (black).

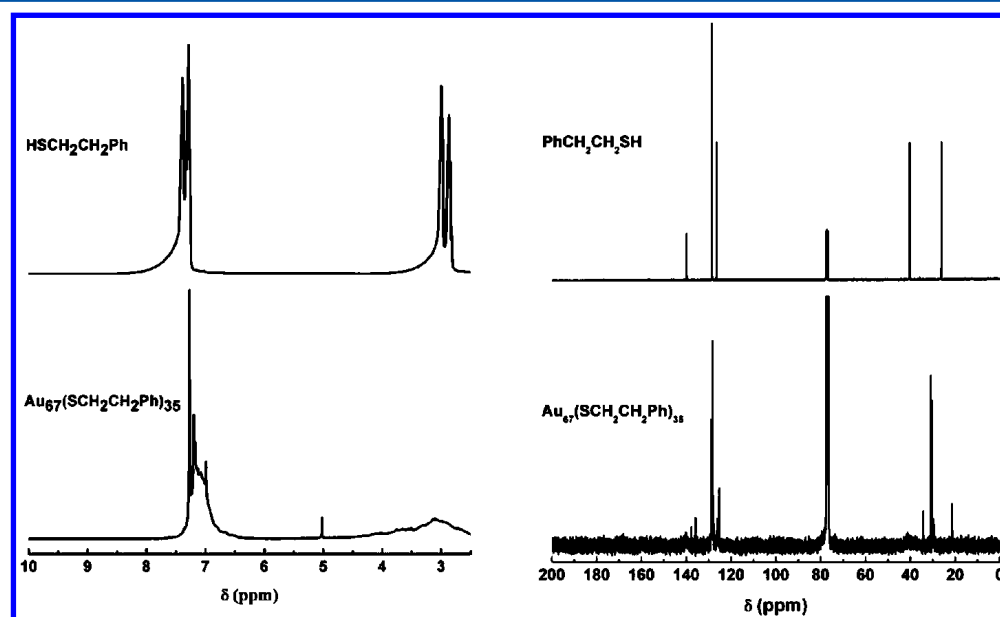**Figure 5.** ^{1}HNMR spectra (left) of monodisperse $Au_{67}(SCH_2CH_2Ph)_{35}$ compared with that of pure thiol ($PhCH_2CH_2SH$) as reference in CDCl$_3$. ^{13}C NMR spectra (right) of monodisperse $Au_{67}(SCH_2CH_2Ph)_{35}$ compared with that of pure thiol ($PhCH_2CH_2SH$) as reference in CDCl$_3$.

broadened or shifter much from their reference positions. NMR spectroscopy also serves as a tool in determining the purity of the compound. The presence of starting materials that are used during the course of synthesis can be detected in the NMR spectrum. Absence of peaks corresponding to the starting materials and impurities indicates good postsynthetic work up of the product.

Evidence relating to the *structure of the gold core* of $Au_{67}(SR)_{35}$ has been obtained by *powder X-ray diffraction*, as described in the Methods. The XRD pattern shown in Figure 4b thus gives information on the lattice structure patterns in the gold core of the nanomolecule. The observed pattern in Figure 4b is substantially in agreement with the one discussed by Cleveland et al.,[25] and explained in terms of a Marks-type truncated decahedral morphology and atom-packing. This direct structural evidence, and its relation to structural

analysis,[45] is crucial in deciding among plausible detailed structural models, as discussed in the Theory below.

Discussion of Experimental Results. In the 1990s, the characterization of gold nanomolecules has been mostly restricted to optical properties, NMR spectroscopy and electrochemistry. In a seminal report, mass spectrometry was used to estimate the number of metal atoms in a series of nanoparticles, including the one denoted as "14-kDa core mass", referring to the inorganic core, which according to the present determination would have a nominal mass of 14 320 Da (67 Au +35 S atoms).[1] But the more recent improvements in mass spectrometry LDI−MS,[46,47] FAB-ion−MS,[48] MALDI−MS[15,27,49,50] and ESI−MS/MS[34,51] have revolutionized this field offering unprecedented molecular weight information on nanoparticles. Electrospray Ionization or ESI is a soft ionization technique which enables the precise compositions with intact metal core and surface thiolate ligands.[31,34,52−54] ESI−MS often
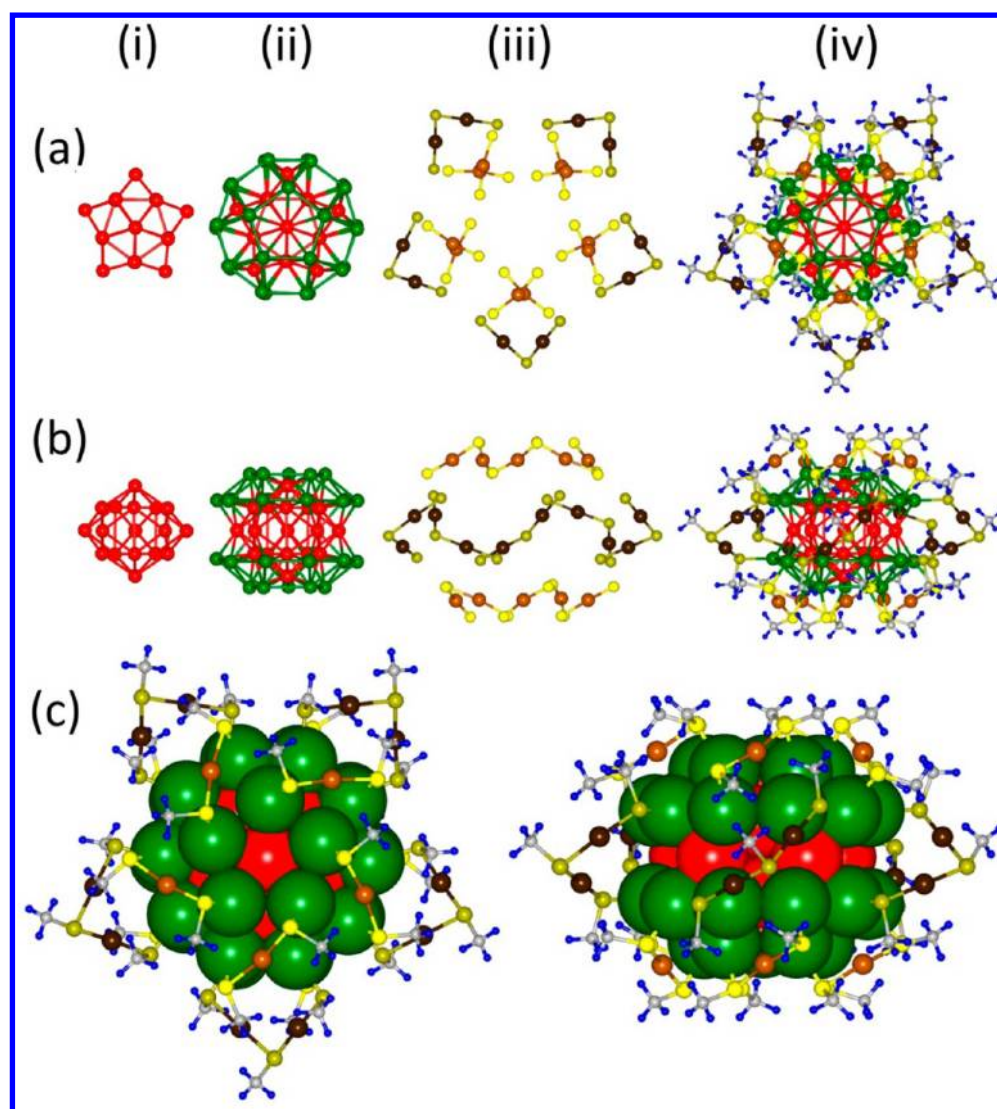
Figure 6. DFT- Optimized atomic structure of the $Au_{67}(SCH_3)_{35}{}^{2-}$. The top two rows (a and b) show two views of the shell-by-shell structures, following the model construction steps in the text. The view in part a is along the 5-fold axis passing through the atom at the vertex of the mDh and normal to its pentagonal planes, and the view in part b is along an axis that is normal to the one used in part a. In columns i–iv, we display for the two views four stages in the construction of the protected cluster, with the complete $Au_{67}(SCH_3)_{35}{}^{2-}$ cluster shown in column iv, as well as in part c, where the structure on the left is the same as the one in part a,iv, and the structure on the right corresponds to that shown in part b,iv. The following structure-building elements are depicted: (i) the 17 Au atom gold mDh (gold atoms in red); (ii) the mDh with the addition of the two pentagonal 15 Au atom caps (in green), forming the Au_{47} (17 + 2 × 15 = 47) core of the protected cluster; (iii) the 10 short (−S−Au−S−) staples (gold atoms in brown and sulfur in bright yellow), and five long (−S−Au-S−Au−S−) staples (gold atoms in black and sulfur in green-mustard color). In part b,iii, the long staples are located between the upper and lower rows which contain the short staples. In both parts a,iii and b,iii, the staples are drawn in the configuration and orientation that they take when attached to the 47-Au atom core to form the protected $Au_{67}(SCH_3)_{35}{}^{2-}$ cluster (see parts a,iv, b,iv, and c). In the figures for the protected cluster the C atoms of the −CH$_3$ groups are shown as small light gray balls, and the hydrogen atoms as smaller blue spheres. For further details, including values of interatomic distances in model I, as well as for atomic structure images for model structure II, see Supporting Information, section TH1.

shows multiply charged peaks, and therefore offers both higher resolution and accuracy. But the compounds need to bear an intrinsic charge in order for electrospray process to generate good signal. In this regard, it is somewhat biased and unreliable in analyzing a mixture of species quantitatively. MALDI−TOF−MS has limited resolution—primarily due to the limited flight tube length—but it has been routinely used to semiquantitatively estimate the contents of any mixture[27] of gold nanomolecules using the special aprotic matrix, DCTB, when operating at higher laser fluence. When the instrument is operated at a lower threshold laser fluence, molecular ions are often obtained that can also be useful for assigning composition

up to a certain mass, ∼10 000 Da. Ultimately, this technique is most useful for rapid monitoring of the synthesis,[27] ligand exchange[55,56] and thermochemical treatment[49] reactions of gold nanomolecules. Its advantages include (a) the minute sample required, usually ∼0.2 mg, for multiple MALDI sample spots in repeated sample data acquisition; (b) the simple and rapid, ∼ 5 min, sample preparation involved in this analysis; and (c) the robustness of data acquisition compared to ESI. Parts a and b of Figure 2 show the MALDI−TOF mass spectra of the purified title compound showing 1+ peaks for phenylethanethiolate (light blue curve) and *n*-hexanethiolate (light red curve) ligands. In contrast to our earlier work,[26] here

the purified sample does not contain significant fraction of Au_{25} or Au_{102} corresponding to 7.4 or ~26 kDa mass, respectively.

An assignment was made in an earlier 2009 report,[26] solely based on MALDI−TOF−MS analysis. In that report, the mass range where molecular ions of nanoparticles can be observed in MALDI was extended to ~18 kDa for the first time, from the previous highest available mass of ~8 kDa (ref 15). MALDI−TOF data was considered adequate to unequivocally demonstrate the existence of the new species at ~18 kDa. The largest nanomolecule studied by high resolution ESI−MS at that time was $Au_{25}(SR)_{18}$ (refs 32 and 54). Shortly after, improved ESI mass spectrometry analysis of the larger nanomolecules 36 kDa, $Au_{144}(SR)_{60}$ (refs 57 and 58) and the 76.3 kDa size,[8,9] has facilitated high resolution ESI analysis of the title compound.

High resolution ESI−MS analysis of the title compound (Figure 2a,b) prepared using distinct −SR ligands (−SCH_2CH_2Ph and −SC_6H_{13}) shows that the correct composition is $Au_{67}(SR)_{35}$. This is confirmed further by obtaining identical molecular ion peaks (Figure 2c) for both the positive and negative ion modes, indicating the absence of any counterions. The number of ligands is calculated from the high resolution mass analysis of the title compound protected by two different thiolate ligands, Figure 2d, and was found to be 35 thiolates. From the number of ligands, the total number of gold atoms was calculated as 67. Subsequent work on using MALDI−TOF−MS data for assignment purposes in our laboratory has been limited; its use has been restricted to ions that are smaller than 12 kDa such as $Au_{36}(SR)_{23}$, $Au_{40}(SR)_{24}$, or $Au_{38}Ag_{38-x}(SR)_{24}$ clusters.[29,49,55,56,59,60] For nanomolecules >12 kDa, we routinely use ESI−MS for accurate mass determination as in the case of $Au_{144}Ag_{144-x}(SR)_{60}$ and the 76 kDa clusters.[8,61] It is clear that a combination of MALDI−TOF and ESI−MS data is preferred for accurate and highly confident compositional assignment.[8,31,57,58,61,62]

Voltammetry of molecule-like nanoparticles show an electrochemical energy gap, which is the difference between the first oxidation and first reduction potentials. When corrected for charging energy, this energy gap is a rough estimate of the HOMO−LUMO band gap that can be correlated to the optical band gap.[3] The size dependent trend of the electrochemical band gap has been reported with Au_{25}, Au_{38}, and Au_{144} showing electrochemical gaps of 1.6, 1.2, and 0.3 V respectively. The 0.74 V gap of Au_{67} reported here fits between the Au_{38} and Au_{144} as expected. Other clusters size of identical band gap of 0.74 V has been reported before.[2,63] Specifically one report with tentative assignment of Au_{75}, reports not only identical band gap of 0.74 V, but also similar features with three oxidation and reduction waves.[63] These occur at different redox potentials than the current work, but this is due to the use of quasi Ag wire as a reference electrode. Here we used Ag/AgCl electrode for the reference electrode. In essence there is a good match between the electrochemistry and the featureless optical spectrum of "Au_{75}" and Au_{67}. Since the "Au_{75}" was published in 2005, when high resolution mass spectrometry for nanoparticles were not well established, it is likely that "Au_{75}" is essentially related to the compounds here demonstrated as Au_{67}.

NMR spectroscopy can provide information about the surface bonding including the Au(I)−thiolate staple units [−SR−Au−SR−] and [−SR−Au−SR−Au−SR−] believed to be the dominant motif in various nanomolecules and also at extended surfaces. High resolution NMR spectroscopy has been shown to identify the number of inequivalent sites, where the number of inequivalent sulfur head groups in a structure corresponds to the number of distinct ligand environments.[64] However, higher resolution and better sensitivity than one presented here is required to perform this type of definitive analysis on Au_{67}.

■ THEORETICAL RESULTS: STRUCTURAL MODEL AND FIRST-PRINCIPLES ANALYSIS

Having established a definite composition of 67 Au atoms and 35 thiolate groups, the question arises as to what kind of structure and bonding this compound must have in order to account for its high stability or selective formation. Previous X-ray scattering experiments[25] on size-selected gold thiolate clusters with core-mass in the 14 kDa range were interpreted in terms of structures of the truncated-decahedral motif, which have 5-fold symmetry accompanied by a certain degree of strain to which the scattering functions are quite sensitive. The particular structures proposed[25] in 1997, were of the (re-entrant, concave) Marks-decahedral (mDh) subclass (for an early description of the mDh, see ref 65), and had either 75 or 73 Au atoms, but the thiolates were assumed to be external, and might number in the 35−40 range. A decade later the mDh structure motif has been established for the 79-atom core of the $Au_{102}(pMBA)_{44}$ cluster (a cluster compound with a core mass of 21 kDa), through total structure determination using single-crystal X-ray diffraction.[11]

Our construction of a structure model for the $Au_{67}(SR)_{35}$ is guided by the above findings, combining the 5-fold mDh motif for a core that is commensurably protected by staple units. The structure models considered have the following features:

(i) The inner core is a 17-atom (minimal) mDh structure, i.e., a pentagonal prism that has been capped on all seven faces; the top and bottom pentagons are, each, capped by a single atom, and one atom caps each of the five rectangular sides (see top and side views in Figure 6a,i and 6b,i)

(ii) A 30-atom shell encapsulates this inner core. It is comprised of two pentagonal 15-atom caps,[65] at opposite poles (top and bottom, see Figure 6, parts a,ii and b,ii, in green), identical to that known for the structure of the 79-atom core of the $Au_{102}(pMBA)_{44}$ cluster.[11,45a] This completes the core part comprised of 17 + 30 = 47 atoms. This 47-atom core differs from the earlier report[26] that proposed a 49-atom (19 + 30) core, in that it lacks two central atoms, leading to a hollow 17-atom core.

(iii) Short stapling units are arranged in a pinwheel fashion over the two polar caps, i.e. five for each cap. These are anchored (stapled) to 10 of the 15 atoms of each cap, leaving unoccupied the remaining five from the periphery of each cap. This accounts for another 10 Au atoms, for a subtotal of 57 of the 67, as well as 20 of the 35 thiolates. See illustration in Figure 6, parts a,iii and b,iii, as well as part c; in these figures the gold atoms in the short (−S−Au−S−) staples are depicted in brown and the sulfur in bright yellow).

(iv) Long stapling units form a belt linking the two polar caps (see in particular the side views in Figure 6b,iii and the right configuration in Figure 6c. Specifically, five such units are anchored (stapled) at each end to one of the above-mentioned peripheral Au atoms of the caps, such that all 30 surface atoms of the core serve as unique

anchoring points. The five long staples account for 10 Au atoms and 15 thiolates, completing the grand total of 67 Au atoms and 35 thiolates.

Several structural variants can be constructed, all preserving the 5-fold rotational symmetry of the mDh core. Indeed, we have considered such variants, which differed in the specific S-anchoring of the long staples to the periphery Au atoms of the polar caps (for details see Supporting Information, section TH1). All the structural variants have been structurally optimized (relaxed to minimize the total energy) with the use of first-principles density-functional (DFT) calculations. The one displayed in Figure 6 (which we refer to as model I) is favored due to its low total energy, remarkably large energy gap (0.75 eV) between the highest (lowest) occupied (unoccupied) molecular orbitals, HOMO (LUMO) (see Figures 7 and 8, below) and the superior correspondence between the measured and calculated X-ray scattering function (see Figure 9, below).
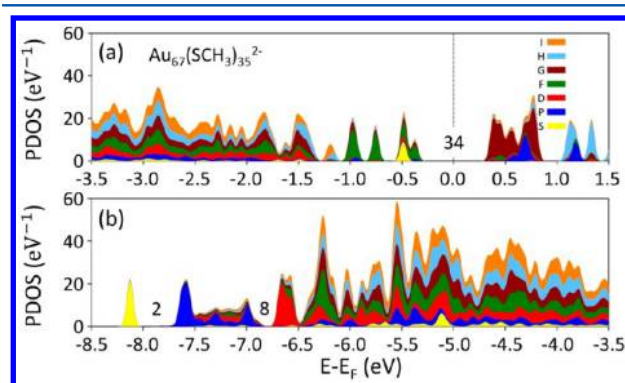

Figure 7. Calculated projected densities of states (PDOS) for $Au_{67}(SCH_3)_{35}^{2-}$. In the PDOS different colors (see the color code at the right of part a) correspond to the various angular momentum contributions, S (0), P (1), D (2), F (3), G (4), H (5), and I (6), which designate the irreducible representations of the full rotation group, SO(3); the numbers in parentheses denote the angular momenta L = 0, 1, 2, ..., with the number of states being $2L+1$ for a given L (that is a maximum of $2(2L+1)$ electrons occupying states of a given angular momentum). The numbers (2, 8, 34) in the PDOS denote the number of electrons occupying superatom shells corresponding to shell closures. Note the large 34 electron energy gap.

Insights into the electronic structure and stability of the protected gold cluster studied here have been gained through first-principles calculations using the spin density-functional theory (SDFT) and employing the ab initio Born–Oppenheimer molecular dynamics, AIBOMD, method which has been originally formulated,[66] and is especially advantageous, for treating charged systems, since it does not employ a supercell; that is, the ionic system is not periodically replicated and consequently no spurious contributions from image multipole interactions are encountered. In this method the Kohn–Sham equations are solved in conjunction with nonlocal norm-conserving soft pseudopotentials[67] (using scalar relativistic ones for the Au atoms), with the valence $5d^{10}$ and $6s^1$ electronic states of the Au atoms, as well as the valence electrons of the S ($3s^2$, $3p^4$), C ($2s^2$,$2p^2$) and hydrogen atoms of the protecting layer, expanded in a plane-wave basis with a 62 Ry kinetic energy cutoff. The Perdew–Burke–Ernzerhof (PBE) functional is employed in the generalized gradient approximation (GGA) to the exchange-correlation corrections.[68]
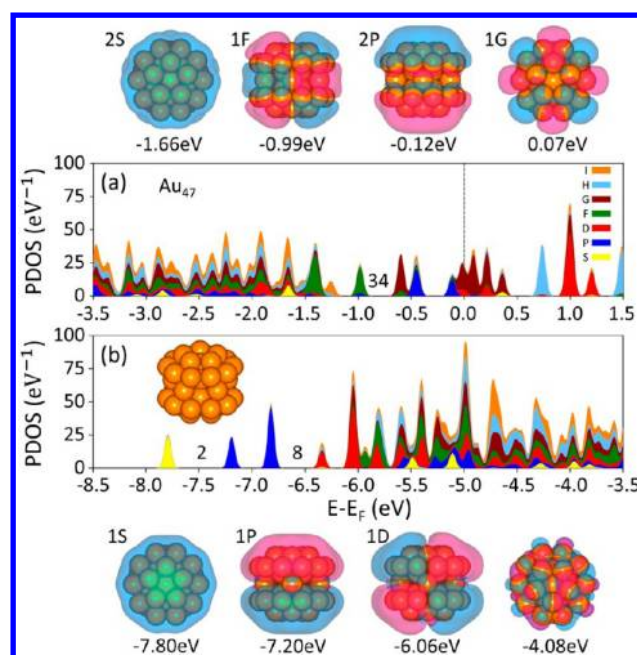

Figure 8. Calculated projected densities of states (PDOS) for the optimized structure of the (bare) Au_{47} core (with the atomic structure displayed as an inset, on the left, in part b). At the top and bottom of electronic spectrum, we show images of selected superatom (delocalized) orbitals, with their energies and angular momenta noted. (blue and pink colors correspond to opposite signs of the wave functions). Also displayed (at the bottom right) is an atom-localized orbital (with energy E-E_F = −4.08 eV), made of Au 5d atomic states. Superatom shell closures are denoted by numbers n^* = 2, 8, and 34. Note that no gap opens at $E − E_F$ = 0, with the vertical dashed line in part a, separating occupied (on the left) and unoccupied (on the right) states, lying inside a band of states of 1G (L = 4, character). For other details see caption of Figure 7.
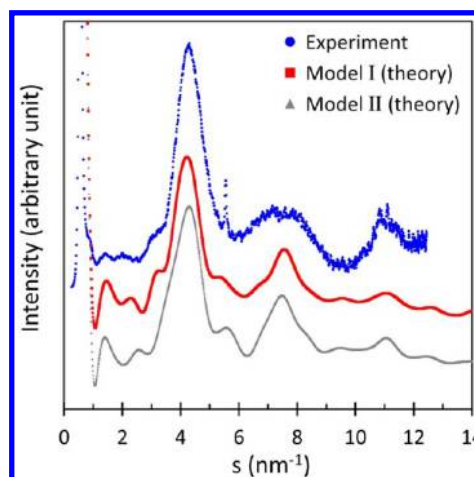

Figure 9. Powder X-ray scattering intensity, calculated with the use of the Debye formula for the optimized structure of $Au_{67}(SCH_3)_{35}^{2-}$ (see Figure 6). The measured data is plotted as $sI(s)$ vs s (in blue). The calculated scattering intensities $I(s)$ vs s, for structural models I (see Figure 6) and II (see Figure SI, Supporting Information TH1), are plotted under the experimental curve. The better agreement (mainly in peak location, see in particular the onset feature near s = 3 nm^{-1}) of the scattering profile calculated for model I (red curve) is evident upon inspection.

In Figure 7 we show the projected densities of states, PDOS (that is, the density of states projected onto the angular

momentum components, introduced first in ref 69; see Supporting Information, section TH2), calculated for the optimized model I structure (see Figure 6) of the $Au_{67}(SCH_3)_{35}^{2-}$ cluster; a vertical dashed line at $E - E_F = 0$ denotes the location of the midpoint between the HOMO and LUMO states of the cluster. The PDOS calculated for the optimized (bare) Au_{47} core is shown in Figure 8.

Inspection of the electronic structure of the cluster (Figures 7 and 8) and the orbitals' angular momenta symmetries (displayed for the cluster core in Figure 8) shows that, in agreement with an early proposal (introduced first in ref 69, termed as a "partial jellium" model, and subsequently used extensively in studies of protected metal clusters[6,13]), the orbitals of states with energies near the top and bottom of the electronic spectra are of delocalized character, derived mainly from the atomic Au $6s^1$ electrons (see representative orbital images in Figure 8). On the other hand, for a wide range of energies (located at the middle of the energy spectrum) the electronic wave functions exhibit localized character (associated with the filled atomic Au $5d^{10}$ states); compare the above delocalized nature of the superatom orbitals with the localized nature of those derived from the 5d electrons of the Au atoms—see in particular the orbital at $E = -4.08$ eV at the bottom of Figure 8b. The delocalized states can be assigned particular symmetries (determined with the use of an expansion of the calculated wave functions in spherical harmonics (see Supporting Information, section TH2)) following the electronic cluster-shell-model (CSM), with a (superatom) aufbau rule: $1S^2 \mid 1P^6 \mid 1D^{10} \mid 2S^2 \; 1F^{14} \mid 2P^6 \; 1G^{18} \mid 2D^{10} \; 1H^{22} \; 3S^2 \mid 1I^{26}...$, where S, P, D, F, G, H, and I, correspond, respectively, to angular momenta, $L = 0, 1, 2, 3, 4, 5,$ and 6. In the above CSM scheme, the vertical lines denote shell-closures (magic numbers), with each closure accompanied by the opening of a stabilizing energy gap; in the above shell-structure scheme the shell closures occur at $n^* = 2, 8, 18, 34, 58, 92, ...,$ electrons (with the values of n^* called "magic numbers").

The order of filling of the delocalized orbitals—those with simple character as indicated by a single color in Figure 7—is largely in accord with this aufbau scheme. This is particularly true where it matters most, i.e. within the ~3 eV range centered about the highest occupied and lowest unoccupied levels, coinciding with the 34-electron magic number. The relatively high position of the 2S orbital (within the 1F manifold of the HOMO complex) and the 2P orbitals (within the 1G manifold of the LUMO complex) may be attributed to a special feature of the proposed structures, namely the lack of a central atom. In fact, the inner core may be regarded either as a cage of 12 atoms, as in the $Au_{144}(SR)_{60}$ model structure,[70] or a cage of 17 atoms.[71]

Deviations from spherical symmetry can cause certain alterations in level ordering, as well as splittings of the $(2L + 1)$-fold level degeneracy by crystal-field effects. Such features are seen clearly in Figures 7 and 8. We highlight in particular the splitting of the seven 1F orbitals (holding 14 electrons) which, together with the $2S^2$ orbital, make up the HOMO complex at the top of the spectrum (-1.0 eV $< E < 0$) of the $Au_{67}(SCH_3)_{35}^{2-}$ cluster, with the 1F states exhibiting a "pseudo-degeneracy" pattern of 3:2:1:1. Crystal-field splitting is exhibited also in the LUMO complex which consists of $1G^{18}$ ($0 < E < 1.0$ eV) states together with the $2P^6$ orbitals (see Figure 7a). A principal cause of the observed splittings may be found in an overall shape change in the effective potential from globular (spherical) to ellipsoidal, either oblate or prolate,

which is sufficient to generate a manifold of $(L + 1)$-levels from the original $(2L + 1)$-fold degenerate one. If oblate, then the lowest level is 2-fold degenerate, and the highest is non-degenerate, which appears to be in better accord with that found (see Figure 7). The reduction in rotational symmetry to that of the atomic framework (symmetry no higher than D_5) produces no further splittings beyond what may be expected from the controlled uncertainties in the optimized structure. Indeed, inspection of the orbital energies reveals a large number of 2-fold effective degeneracies (within ± 0.01 eV), indicating that the rotational symmetry is well preserved.

The gap itself is slightly greater than 0.75 eV, which compares well with the onset of strong optical absorption first reported[2] in 1998. In their analysis of the optical response of 14 kDa class thiolate-protected gold clusters, the authors of that study identified an optical absorption onset near 0.6 eV, a rapid rise to stronger absorption centered near 0.9 eV, and a first peak or plateau reached at 1.1 eV. This is in broad accord with a calculated HOMO−LUMO gap of 0.75 eV separating states of (superatom) 1F and 1G character, and a separation of ca. 1.2 eV (i.e., from −0.6 to +0.6 eV) between the centroids of the HOMO and LUMO complexes. Further spectroscopic measurements, at low temperature, and theoretical work, to obtain precise estimates of the energies and transition moments between the ground state and excited states, will be required to make a comprehensive quantitative comparison between experiment and theory.

The main feature in the electronic spectrum of the $Au_{67}(SCH_3)_{35}^{2-}$ cluster is the large HOMO−LUMO energy gap, $\Delta_{HL} = 0.75$ *eV*, corresponding to a superatom shell closing at 34 electrons (see below) of the dianion cluster. This large gap confers high stability to the cluster, endowing it with resistance to chemical attack. Also noted are shell-closure energy gaps at 2 and 8 electron fillings, while the one corresponding to $n^* = 18$ is obscured due to mixing with localized atomic orbitals (of d character) having similar energies to the superatom 1D states. Additional insight into the origins of the electronic stabilization of the cluster may be gained from inspection of the PDOS in Figure 8, calculated for the optimized geometry of the Au_{47} core (see see inset in Figure 8b). Inspection of the figure reveals that while the aforementioned shell closures observed for the dressed cluster are preserved (albeit the one at 34 electrons is notably smaller), no superatom stabilization gap occurs at $E = E_F$; nor can such gap be opened by varying the number of electrons of the cluster (namely charging of the cluster) within a reasonable range. This leads us to conclude that despite the compact nature of the Au_{47} core and its clear superatom orbital characters (see orbital images in Figure 8), by itself the core does not possess special stability. Instead, it is the integral system (i.e., compact core encapsulated by a more loosely packed protective shell) which acquires the requisite stabilization through engagement of the appropriate number of "core electrons" by the anchored staples (one electron for each of the 15 staples) resulting in the 47−15 + (2) = 34 electron gap observed for the in Figure 7a).

Added support for the structural model is obtained from comparisons between the measured and calculated (using the Debye formula,[72] see Supporting Information section TH3) powder X-ray scattering intensities shown in Figure 9 for optimized structures of $Au_{67}(SCH_3)_{35}^{2-}$ (see Figure 6). The measured data is plotted as $s\,I(s)$ vs s (in blue). Focusing on peak locations, comparisons between the measured intensities and the profiles ($I(s)$ vs s) calculated for optimized structure

models I (red curve in Figure 9) and II (gray curve in Figure 9), show close correspondence, with better agreement observed for model I (see in particular the peak onset feature near s = 3 nm^{-1}).

Many features of the X-ray scattering function are well accounted for by any of the optimized (67,35) structure models, e.g. the shape-factor minima located in the small-angle region.[45b] This indicates merely that the strongly scattering core is a globular shape with an effective diameter equivalent to that of ∼70 closely packed Au atoms. Model I is judged to be uniquely satisfactory in accounting for the X-ray scattering in the principal peak region, i.e. from 3 to 6 nm^{-1}, which correspond to (111) and (200) bulk atomic-lattice reflections, located at 4.26 and 4.90 nm^{-1}, respectively. The model predicts pedestal-like shape for this region, with a step up starting near 3.2 nm^{-1} and a step down starting near 5.4 nm^{-1}. The other structural variants predict either distinct peaks in these regions, well separated from the principle peak, or as broadened shoulders blended into the principal peak. For a critical comparison of the small-angle region (<2.5) and the large-angle region (>6.5 nm^{-1}), further work to improve respectively the crystallinity and the signal-to-noise will be required. The clear superiority of model I over the other candidates attempted (optimized) indicates that it is the connectivity (or bonding network) that can be a decisive factor. This is because the "coordination sphere", or nearest-neighbor environment, is essentially identical in all models, disregarding the so-called "aurophilic" attractions between staple-motif's Au(I) sites and the core.

The above illustrates the advantage of using multiple (experimental and theoretical) approaches for structural determination of larger noble metal cluster compound (made of gold as well as other nobel metals, see, e.g., ref 73 on the structure of a Pd$_{145}$ compound which served as a source of inspiration for the work in ref 70).

Charging of the cluster (by increasing or depleting the number of electrons) may be described in terms of the addition energy, $E_{add,N}$, of a cluster with N electrons, given as the second difference of the total energy of the cluster[74]

$$E_{add,N} = E_{N+1} - 2E_N + E_{N-1} \quad (1)$$

where E_N is the total energy of the cluster with N electrons. The addition energy may be written as $E_{add,N} = I_N - A_N$, where the ionization energy is given as $I_N = E_{N-1} - E_N$, and the electron affinity as $A_N = E_N - E_{N+1}$. In our calculations we consider adiabatic ionization and electron affinities, namely, the nuclear positions are relaxed (optimized via energy minimization) after each change in the charge state of the cluster. The equilibrium state of the protected gold cluster considered here is the dianionic state, $Au_{67}(SR)_{35}{}^{2-}$, i.e. the number of electrons in the equilibrium cluster is N + 2. In the following we denote the charge state of the cluster as z = −2 + q, where q is an integer q = ..., −2, −1, 0, 1, 2, ...; charge states with q > 0 correspond to oxidized states with respect to the equilibrium state z = −2 (q = 0), and states with q < 0 are reduced states with respect to the one with z = −2. Calculated values for $E_{add,N}(z)$, $I_N(z)$ and $A_N(z)$ are given in Table 2; here $E_{add,N}(z)$ is the addition energy for a cluster with N−z electrons and the same for $I_N(z)$ and $A_N(z)$.

The results of our first-principles calculations for the total energy difference between oxidized and reduced states of the cluster, expressed as the energy difference $\Delta E_N(z) = E_N(-2) - E_N(z)$, where $E_N(z)$ is the total energy of the cluster with N − z

Table 2. Calculated Values for the Addition Energies, $E_{add,N}(z)$, Adiabatic Ionization Energies, $I_N(z)$, and Adiabatic Electron Affinities, $A_N(z)$, for Different Cluster Charge-States, z^a

z	EA (eV)	IP (eV)	E_{add} (eV)
0	3.06		
−1	1.41	3.06	1.65
−2	−0.30	1.41	1.68
−3	−1.18	−0.30	0.91
−4		−1.18	

^{a}Here, z = −2 is the equilibrium (reference) state.

= N + 2 − q electrons, plotted as a function of z, are shown in Figure 10. The line gives a quadratic fit to the calculated values.
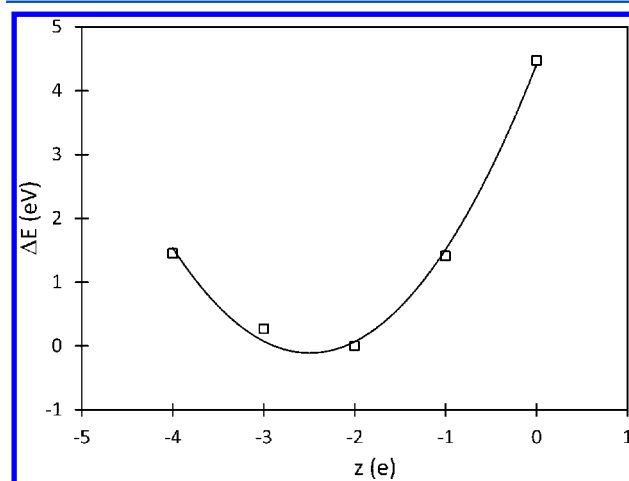

Figure 10. Energy difference $\Delta E_N(z) = E_N(-2) - E_N(z)$, where $E_N(z)$ is the total energy of the cluster with N − z = N + 2 − q (q = ..., −2, −1, 0, 1, 2, ...) electrons, plotted as a function of z; z is the charge state of the $Au_{67}(SCH_3)_{35}{}^{z-}$ cluster. The line gives a quadratic fit to the calculated values. The coefficient of the quadratic term of the fit gives an estimate for the effective capacitance of the protected cluster, C = 0.11 aF (1 aF = 10^{-18} F); the charging energy of the cluster is given by $E_{ch} = e^2/C$.

The coefficient of the quadratic term of the fit in Figure 10 gives an estimate for the effective capacitance of the protected cluster, C = 0.11 aF (1 aF = 10^{-18} F); the charging energy of the cluster is given by $E_{ch} = e^2/C$. The rather adequate (quadratic) fit indicates metallic-like charging behavior. Comparisons between these results and the voltammetry measurements discussed above are outside the scope of this work, since the measured values are governed, in addition to the properties of the cluster itself, by a number of factors[3] that are not considered in the calculations. These include the dielectric properties of the solvent, penetration of electrolyte ions into the protecting thiolate layer, and the precise nature of the thiolate layer (modeled by us here as −SCH$_3$).

■ CONCLUSIONS

We report the high yield synthesis and composition determination of $Au_{67}(SR)_{35}$, a nanomolecule lying between the superstable 38- and 144- atom cores, identified using high resolution ESI mass spectrometry. The THF solvent mediated synthesis, employing phenylethanethiolate ligand yielding the title compound has been reproduced over one hundred times in our laboratory among various researchers spanning a four year

time period. Multiple techniques were used to characterize the title gold nanomolecule. Electronic properties were explored using optical absorption spectroscopy (UV−visible−NIR regions) and electrochemistry (0.74 V spacing in differential-pulsed-voltammetry), modes of ligand binding were studied by NMR spectroscopy (^{13}C and ^{1}H), and structural characteristics of the metal atom core were determined by powder X-ray measurements. The electronic structure of the cluster was analyzed with the use of first-principles DFT calculations, interpreted within the framework the superatom shell model. The main feature in the electronic spectrum of the $Au_{67}(SCH_3)_{35}^{2-}$ cluster is the large HOMO−LUMO energy gap, $\Delta_{HL} = 0.75$ eV, corresponding to a superatom shell closing at 34 electrons of the dianion cluster; further experimental work pertaining to the theoretically predicted charge state of the protected cluster is desirable. The observed, and calculated, large gap confers high stability to the cluster, endowing it with resistance to chemical attack.

The definite compositional evidence and augmented structural measurements have been employed to devise structural models that might account for the singular stability and salient properties of these compounds. One of these models has been found to be superior in all these respects, and consequently its stability, electronic structure and bonding, and likely electronic transitions (optical and charging) have been investigated in further detail, to provide deeper insight into this prominent class of compounds. Structurally, the $Au_{67}(SR)_{35}$ nanomolecule is the smallest to adopt the complete truncated-decahedral motif for its core with a surface structure bearing greater similarity to the larger nanoparticles. Its aforementioned electronic energy gap (∼0.75 eV) is nearly double that of the larger Au_{102} compound and it is much smaller than that of the Au_{38} one.

The intermediary status of the $Au_{67}(SR)_{35}$ nanomolecule is also reflected in both its optical and electrochemical characteristics. Indeed, while Au_{144} shows quantized double-layer charging and Au_{38} exhibits molecule-like electrochemical behavior, the electrochemical band gap and optical spectra of Au_{67} show that it is positioned below the onset of metallic behavior. Isolation and characterization of distinct nanomolecules in this size regime and development of a first-principles theoretical framework of interpretive and predictive capability, are indispensable in order to gain deep insights about the transition from "metallic" to "molecular" character.

ASSOCIATED CONTENT

Ⓢ Supporting Information

Reproducibility information, cyclic voltammetry, expanded MALDI−MS results, and NMR and UV−visible data and a description of theoretical methods and supplementary results from the structure modeling and the high level electronic structure theory. This material is available free of charge via the Internet at http://pubs.acs.org.

AUTHOR INFORMATION

Corresponding Author
*E-mail: amal@olemiss.edu.

Author Contributions
All authors made significant contributions to the manuscript. All authors contributed to the writing of the manuscript.

Notes
The authors declare no competing financial interest.

REFERENCES

(1) Whetten, R. L.; Khoury, J. T.; Alvarez, M. M.; Murthy, S.; Vezmar, I.; Wang, Z. L.; Stephens, P. W.; Cleveland, C. L.; Luedtke, W. D.; Landman, U. *Adv. Mater.* **1996**, *8*, 428−433.

(2) Chen, S. W.; Ingram, R. S.; Hostetler, M. J.; Pietron, J. J.; Murray, R. W.; Schaaff, T. G.; Khoury, J. T.; Alvarez, M. M.; Whetten, R. L. *Science* **1998**, *280*, 2098−2101.

(3) Murray, R. W. *Chem. Rev.* **2008**, *108*, 2688−2720.

(4) Schaaff, T. G.; Shafigullin, M. N.; Khoury, J. T.; Vezmar, I.; Whetten, R. L.; Cullen, W. G.; First, P. N.; GutierrezWing, C.; Ascensio, J.; JoseYacaman, M. J. *J. Phys. Chem. B* **1997**, *101*, 7885−7891.

(5) Wyrwas, R. B.; Alvarez, M. M.; Khoury, J. T.; Price, R. C.; Schaaff, T. G.; Whetten, R. L. *Eur. Phys. J. D* **2007**, *43*, 91−95.

(6) Walter, M.; Akola, J.; Lopez-Acevedo, O.; Jadzinsky, P. D.; Calero, G.; Ackerson, C. J.; Whetten, R. L.; Gronbeck, H.; Hakkinen, H. *Proc. Natl. Acad. Sci. U.S.A.* **2008**, *105*, 9157−9162.

(7) Dass, A. *Nanoscale* **2012**, *4*, 2260−2263.

(8) Dass, A. *J. Am. Chem. Soc.* **2011**, *133*, 19259−19261.

(9) Qian, H.; Zhu, Y.; Jin, R. *Proc. Natl. Acad. Sci. U.S.A* **2012**, *109*, 696−700.

(10) Faraday, M. *Philos. Trans. R. Soc. London* **1857**, *147*, 145.

(11) Jadzinsky, P. D.; Calero, G.; Ackerson, C. J.; Bushnell, D. A.; Kornberg, R. D. *Science* **2007**, *318*, 430−433.

(12) Heaven, M. W.; Dass, A.; White, P. S.; Holt, K. M.; Murray, R. W. *J. Am. Chem. Soc.* **2008**, *130*, 3754−3755.

(13) Akola, J.; Walter, M.; Whetten, R. L.; Hakkinen, H.; Gronbeck, H. *J. Am. Chem. Soc.* **2008**, *130*, 3756−3757.

(14) Zhu, M.; Aikens, C. M.; Hollander, F. J.; Schatz, G. C.; Jin, R. *J. Am. Chem. Soc.* **2008**, *130*, 5883−5885.

(15) Dass, A.; Stevenson, A.; Dubay, G. R.; Tracy, J. B.; Murray, R. W. *J. Am. Chem. Soc.* **2008**, *130*, 5940−5946.

(16) Qian, H.; Zhu, Y.; Jin, R. *ACS Nano* **2009**, *3*, 3795−3803.

(17) Häkkinen, H. *Nat. Chem.* **2012**, *4*, 443−455.

(18) Pei, Y.; Pal, R.; Liu, C.; Gao, Y.; Zhang, Z.; Zeng, X. C. *J. Am. Chem. Soc.* **2012**, *134*, 3015−3024.

(19) Jiang, D. E.; Dai, S. *Inorg. Chem.* **2009**, *48*, 2720−2722.

(20) Aikens, C. M. *J. Phys. Chem. C* **2008**, *112*, 19797−19800.

(21) Pei, Y.; Gao, Y.; Zeng, X. C. *J. Am. Chem. Soc.* **2008**, *130*, 7830−7832.

(22) Jin, R. *Nanoscale* **2010**, *2*, 343−362.

(23) Levi-Kalisman, Y.; Jadzinsky, P. D.; Kalisman, N.; Tsunoyama, H.; Tsukuda, T.; Bushnell, D. A.; Kornberg, R. D. *J. Am. Chem. Soc.* **2011**, *133*, 2976−2982.

(24) Schaaff, T. G.; Whetten, R. L. *J. Phys. Chem. B* **1999**, *103*, 9394−9396.

(25) Cleveland, C. L.; Landman, U.; Schaaff, T. G.; Shafigullin, M. N.; Stephens, P. W.; Whetten, R. L. *Phys. Rev. Lett.* **1997**, *79*, 1873−1876.

(26) Dass, A. *J. Am. Chem. Soc.* **2009**, *131*, 11666−11667.

(27) Dharmaratne, A. C.; Krick, T.; Dass, A. *J. Am. Chem. Soc.* **2009**, *131*, 13604−13605.

(28) Wu, Z.; Suhan, J.; Jin, R. *J. Mater. Chem.* **2009**, *19*, 622−626.

(29) Knoppe, S.; Boudon, J.; Dolamic, I.; Dass, A.; Bürgi, T. *Anal. Chem.* **2011**, *83*, 5056−5061.

(30) Tsunoyama, H.; Negishi, Y.; Tsukuda, T. *J. Am. Chem. Soc.* **2006**, *128*, 6036−6037.

(31) Chaki, N. K.; Negishi, Y.; Tsunoyama, H.; Shichibu, Y.; Tsukuda, T. *J. Am. Chem. Soc.* **2008**, *130*, 8608−8610.

(32) Tracy, J. B.; Crowe, M. C.; Parker, J. F.; Hampe, O.; Fields-Zinna, C. A.; Dass, A.; Murray, R. W. *J. Am. Chem. Soc.* **2007**, *129*, 16209−16215.

(33) Negishi, Y.; Chaki, N. K.; Shichibu, Y.; Whetten, R. L.; Tsukuda, T. *J. Am. Chem. Soc.* **2007**, *129*, 11322−11323.

(34) Angel, L. A.; Majors, L. T.; Dharmaratne, A. C.; Dass, A. *ACS Nano* **2010**, *4*, 4691−4700.

(35) Even though the Au_4L_4 loss in MALDI−TOF remains valid as discussed in our earlier report (see ref 26), we believe that the previous assignment was erroneous due to calibration error in MALDI−TOF−MS.

(36) Alvarez, M. M.; Khoury, J. T.; Schaaff, T. G.; Shafigullin, M. N.; Vezmar, I.; Whetten, R. L. *J. Phys. Chem. B* **1997**, *101*, 3706−3712.

(37) Hicks, J. F.; Miles, D. T.; Murray, R. W. *J. Am. Chem. Soc.* **2002**, *124*, 13322−13328.

(38) Quinn, B. M.; Liljeroth, P.; Ruiz, V.; Laaksonen, T.; Kontturi, K. *J. Am. Chem. Soc.* **2003**, *125*, 6644−6645.

(39) Ingram, R. S.; Hostetler, M. J.; Murray, R. W.; Schaaff, T. G.; Khoury, J. T.; Whetten, R. L.; Bigioni, T. P.; Guthrie, D. K.; First, P. N. *J. Am. Chem. Soc.* **1997**, *119*, 9279−9280.

(40) Hicks, J. F.; Templeton, A. C.; Chen, S. W.; Sheran, K. M.; Jasti, R.; Murray, R. W.; Debord, J.; Schaaf, T. G.; Whetten, R. L. *Anal. Chem.* **1999**, *71*, 3703−3711.

(41) Guo, R.; Georganopoulou, D.; Feldberg, S. W.; Donkers, R.; Murray, R. W. *Anal. Chem.* **2005**, *77*, 2662−2669.

(42) Su, B.; Zhang, M.; Shao, Y.; Girault, H. H. *J. Phys. Chem. B* **2006**, *110*, 21460−21466.

(43) Holm, A. H.; Ceccato, M.; Donkers, R. L.; Fabris, L.; Pace, G.; Maran, F. *Langmuir* **2006**, *22*, 10584−10589.

(44) Terrill, R. H.; Postlethwaite, T. A.; Chen, C.-H.; Poon, C.-D.; Terzis, A.; Chen, A.; Hutchison, J. E.; Clark, M. R.; Wignall, G. *J. Am. Chem. Soc.* **1995**, *117*, 12537−12548.

(45) (a) Mednikov, E. G.; Dahl, L. F. *Small* **2008**, *4*, 534−537. (b) Whetten, R. L.; Shafigullin, M. N.; Khoury, J. T.; Schaaff, T. G.; Vezmar, I.; Alvarez, M. M.; Wilkinson, A. *Acc. Chem. Res.* **1999**, *32*, 397−406.

(46) Wu, Z.; Gayathri, C.; Gil, R. R.; Jin, R. *J. Am. Chem. Soc.* **2009**, *131*, 6535−6542.

(47) Schaaff, T. G.; Shafigullin, M. N.; Khoury, J. T.; Vezmar, I.; Whetten, R. L. *J. Phys. Chem. B* **2001**, *105*, 8785−8796.

(48) Dass, A.; Guo, R.; Tracy, J. B.; Balasubramanian, R.; Douglas, A. D.; Murray, R. W. *Langmuir* **2008**, *24*, 310−315.

(49) Nimmala, P. R.; Dass, A. *J. Am. Chem. Soc.* **2011**, *133*, 9175−9177.

(50) Reilly, S. M.; Krick, T.; Dass, A. *J. Phys. Chem. C* **2010**, *114*, 741−745.

(51) Fields-Zinna, C. A.; Sampson, J. S.; Crowe, M. C.; Tracy, J. B.; Parker, J. F.; deNey, A. M.; Muddiman, D. C.; Murray, R. W. *J. Am. Chem. Soc.* **2009**, *131*, 13844−13851.

(52) Schaaff, T. G.; Knight, G.; Shafigullin, M. N.; Borkman, R. F.; Whetten, R. L. *J. Phys. Chem. B* **1998**, *102*, 10643−10646.

(53) Negishi, Y.; Nobusada, K.; Tsukuda, T. *J. Am. Chem. Soc.* **2005**, *127*, 5261−5270.

(54) Tracy, J. B.; Kalyuzhny, G.; Crowe, M. C.; Balasubramanian, R.; Choi, J. P.; Murray, R. W. *J. Am. Chem. Soc.* **2007**, *129*, 6706−6707.

(55) Jupally, V. R.; Kota, R.; Dornshuld, E. V.; Mattern, D. L.; Tschumper, G. S.; Jiang, D.-e.; Dass, A. *J. Am. Chem. Soc.* **2011**, *133*, 20258−20266.

(56) Knoppe, S.; Dharmaratne, A. C.; Schreiner, E.; Dass, A.; Bürgi, T. *J. Am. Chem. Soc.* **2010**, *132*, 16783−16789.

(57) Fields-Zinna, C. A.; Sardar, R.; Beasley, C. A.; Murray, R. W. *J. Am. Chem. Soc.* **2009**, *131*, 16266−16271.

(58) Qian, H.; Jin, R. *Nano Lett.* **2009**, *9*, 4083−4087.

(59) Kumara, C.; Dass, A. *Nanoscale* **2012**, *4*, 4084−4086.

(60) Knoppe, S.; Dolamic, I.; Dass, A.; Bürgi, T. *Angew. Chem., Int. Ed.* **2012**, *51*, 7589−7591.

(61) Kumara, C.; Dass, A. *Nanoscale* **2011**, 3064−3067.

(62) Negishi, Y.; Sakamoto, C.; Ohyama, T.; Tsukuda, T. *J. Phys. Chem. Lett.* **2012**, *3*, 1624−1628.

(63) Balasubramanian, R.; Guo, R.; Mills, A. J.; Murray, R. W. *J. Am. Chem. Soc.* **2005**, *127*, 8126−8132.

(64) Wong, O. A.; Heinecke, C. L.; Simone, A. R.; Whetten, R. L.; Ackerson, C. J. *Nanoscale* **2012**, *4*, 4099−4102.

(65) Cleveland, C. L.; Landman, U. *J. Chem. Phys.* **1991**, *94*, 7376−7396.

(66) Barnett, R. N.; Landman, U. *Phys. Rev. B* **1993**, *48*, 2081−2097.

(67) Troullier, N.; Martins, J. L. *Phys. Rev. B* **1991**, *43*, 1993−2006.

(68) Perdew, J. P.; Burke, K.; Ernzerhof, M. *Phys. Rev. Lett.* **1997**, *78*, 1396−1396.

(69) Yoon, B.; Koskinen, P.; Huber, B.; Kostko, O.; von Issendorff, B.; Häkkinen, H.; Moseler, M.; Landman, U. *Chemphyschem* **2007**, *8*, 157−161.

(70) Lopez-Acevedo, O.; Akola, J.; Whetten, R. L.; Gronbeck, H.; Häkkinen, H. *J. Phys. Chem. C* **2009**, *113*, 5035−5038.

(71) Bulusu, S.; Li, X.; Wang, L.-S.; Zeng, X. C. *Proc. Natl. Acad. Sci. U.S.A.* **2006**, *103*, 8326−8330.

(72) Cleveland, C. L.; Landman, U.; Shafigullin, M. N.; Stephens, P. W.; Whetten, R. L. *Z. Phys. D* **1997**, *40*, 503−508.

(73) Tran, N. T.; Powell, D. R.; Dahl, L. F. *Angew. Chem., Int. Ed.* **2000**, *39*, 4121−4125.

(74) Häkkinen, H.; Barnett, R. N.; Landman, U. *Phys. Rev. Lett.* **1999**, *82*, 3264−3267.